PAPER

Effect of groove curvature on droplet spreading

J. Van Hulle (ID) * and N. Vandewalle (ID)

Capillary transport of droplets through channels and tubes is a well known problem in physics. Many different behaviors and dynamics have been reported so far depending mostly on the geometry of the system. In nature, curved grooves are observed on water-transporting organs of self-watering plants. However, less attention has been dedicated to the curvature effects of the channel transporting the liquid. In this work, we focus on this aspect by experimentally studying droplet spreading on 3D printed grooves with different curvatures. We prove that the sign of the curvature has a major effect on the shape and droplet dynamics. In all cases, the spreading dynamics follow a power law $x = ct^p$. For a concave groove, called hypocycle, the power $p = 1/3$ and the prefactor c increases if the groove's radius decreases. For a convex groove, called epicycle, $p = 1/2$ and c is independent of the groove radius. Two models are proposed to describe the scaling laws. The spreading of a droplet is much faster inside an epicycle groove than in a hypocycle groove, opening ways to develop applications.

1. Introduction

A wetting liquid may spread spontaneously along a surface thanks to capillary driving forces.[1] This spontaneous motion is of primary importance in many fields. Biomedical applications with lab-on-chip devices,[2,3] water delivery in microgravity[4] or also water collection in arid regions.[5] Even in our everyday life, capillarity governs the way a biscuit soaks up coffee or water absorbs into paper.[6]

Several studies have examined capillary rise into different structures, or droplet spreading on specific substrates.[7–10] A general trend has been observed, the position of the advancing meniscus always follows a power law $x = ct^p$, where x is the position of the leading meniscus, t is time. The exponent value p depends on various experimental parameters: whether the volume of liquid is conserved or not, whether the transporting structure is open or closed, it also depends on the shape and size of this transporting structure. A succinct review is provided in Section 4.1. However less attention has been dedicated to the effects of curvature.
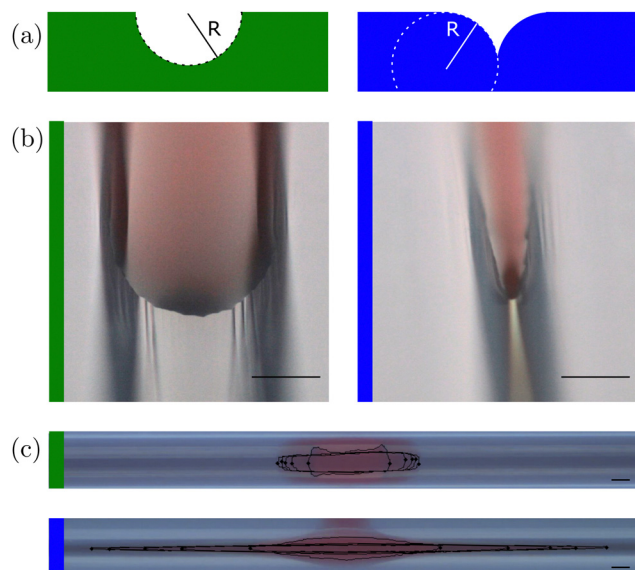
When it comes to efficiency, nature is often a good source of inspiration since natural selection has shaped the best features over time. Plants dealing with water scarcity have developed specific structures to harvest and transport water.[14–16] One can cite the spines of the *Opuntia microdasys* cactus,[11] the trichomes of the insect trapping plant *Sarracenia*[12] and the leaf of the Namib desert grass *Stipagrostis sabulicola*.[13] In Fig. 1, we show a 3D representation of various textures observed on

GRASP, Institute of Physics B5a, University of Liège, B4000 Liège, Belgium.
E-mail: jvanhulle@uliege.be

water-transporting organs of these plants. All organs have an overall conical shape and, along the fiber, one notices curved grooves. The conical geometry is known to passively transport the droplet along the fiber[17–19] as soon as the droplets are captured which increase the water harvesting efficiency.[20–22] Then, the purpose of the grooves is also to enhance the water droplet motion by pre-wetting and keeping wet the fiber.[12] Two recent studies showed that curved grooves on synthetic conical fibers can also increase the liquid transport.[23,24] Notice, from the examples shown in Fig. 1, that curved grooves appear at
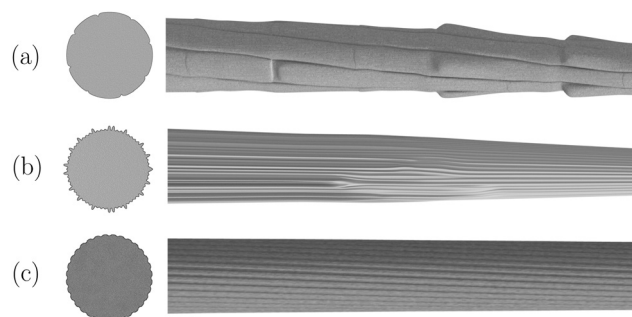
Fig. 1 Representation of natural fibers found on several plants with the expected cross-sections of the fiber. Illustration of (a) a cactus spine observed on *Opuntia microdasys*,[11] (b) a trichome of the insect trapping plant *Sarracenia*,[12] (c) a leaf of the Namib desert grass *Stipagrostis sabulicola*.[13] All these structures are used by the plants to collect and drive water droplets. The ingredients are the same in each case, the fiber is conical and there are curved grooves along the fiber. The diameter of each natural fiber is approximately 35 μm for the *Opuntia microdasys* spine, 40 μm for the *Sarracenia* trichome and 250 μm for the *Stipagrostis sabulicola* leaf.

Fig. 2 (a) Illustration of a hypocycle groove (left) and an epicycle groove (right). (b) Pictures of the liquid front in a hypocycle groove (left) and an epicycle groove (right). The radius of the groove is the same being $R = 1.37$ mm, as sketched above the pictures. The droplet is colored in red. One can observe that the shape of the advancing front of the droplet is impacted by the curvature of the groove. In a hypocycle groove, the droplet has a round advancing meniscus. In an epicycle groove, the droplet is pinched at the bottom of the groove. (c) Superposition of experimental pictures of a red dyed droplet spreading in a hypocycle groove (top) and in an epicycle groove (bottom) with the same radius $R = 1.37$ mm. The numerically found contour is in black. The time interval between successive contour is 5 s. The scale bars represent 1 mm.

different scales. In addition, two types of curved grooves structures are observed. For Fig. 1(a) and (c), the bumps appears wider than the hollows. For Fig. 1(b) the bumps and the hollows have the same width. One can wonder what is the best groove's geometry to spread droplets.

In Fig. 2, we show experimental pictures of a droplet, colored in red, spreading inside a groove. The groove is either concave, called hypocycle, or convex, called epicycle. One can see that the droplet shapes are different. As a consequence, the dynamics of spreading should be deeply affected.

In the present study, we compare the influence of the curvature's groove sign on the spreading dynamics of a droplet. In other words, we are searching for the curvature (convex or concave) that enhances the droplet spreading.

2. Methods

The substrates are three-dimensionally (3D) printed with Object Prime 30 from Stratasys. The printer is jetting tiny polymers droplets which are cured with a UV lamp. The accuracy of a single layer is about 30 μm. The material used by the printer is Acrylonitrile Butadiene Styrene (ABS). The 3D-printing technique allows to tune the curvature's sign as well as the radius R of the groove. We use grooves with R ranging from 0.5 mm to 2 mm. The radius R of the curved groove is sketched in Fig. 2(a). This substrate is

horizontal and a droplet of liquid is gently deposited in the middle of one groove. The droplet is produced by a micropipette (Eppendorf Xplorer). The liquid is silicone oil (Dow Corning) with a viscosity $\nu = 100$ cSt. The surface tension is $\gamma = 20.6$ mN m^{-1} and the density is $\rho = 960$ kg m^{-3}. The droplet volume is fixed at $\Omega = 5$ μL. The static contact angle of silicone oil on ABS is very small, we are thus in the case of total wetting, $\theta_{\rm E} \simeq 0°$. Prior to each experiment, the groove is cleaned with isopropanol and distilled water, then the surface is left to dry.

The droplet spreading is recorded from above thanks to a CCD camera (Charge-Coupled Device) at 20 fps. To improve the contrast as in Fig. 2, silicone oil is colored in red and we used two lights (Effilux) on each side of the groove. With an image treatment, the contour of the spreading droplet over time is detected (see Fig. 2(c)). It allows to obtain the left and right positions of the advancing meniscus and so the spread x of the droplet along the groove. The spreading is recorded after the droplet is completely inside the groove. For a given droplet volume Ω, the droplet completely fills the groove if the spread x is higher than the calculated filled spreading, $x > x_{\rm f} = \Omega/S$ where S is the cross section of the groove. Before the value $x_{\rm f}$ is reached the droplet sits around the groove with a spherical cap. These early stages of droplet spreading will not be described in the present study.

3. Results

When the droplet is in contact with the groove, the spreading becomes one directional. To investigate the crucial physical parameters, one can calculate several adimensional numbers. The capillary number compares surface tension effects to viscous ones, it is defined by Ca = $\dot{x}\nu\rho/\gamma$ where $\dot{x}$ is the speed of spreading, ρ the density and γ the surface tension. In our case, we found Ca $\simeq 2 \times 10^{-3}$ meaning that surface tension overcomes viscosity. The Weber number compares the inertial force to the surface tension force, we have We = $\rho\dot{x}^2 L/\gamma$ with L the characteristic length of the system. In the present study, droplets are confined inside a millimetre groove, so we have $L \simeq 10^{-3}$ m. For our experiments, the Weber number is typically We $\simeq 2 \times 10^{-5}$, meaning that surface tension forces dominate inertial forces. The Reynolds number, Re = $\dot{x}L/\nu \simeq 7 \times 10^{-3}$, compares inertial forces to viscous forces. This value reveals that viscous forces are larger than inertial ones. The Bond number compares gravitational forces to capillary forces, Bo = $\rho g L^2/\gamma \simeq 0.5$, where g is the gravitational acceleration. It indicates that capillary forces are larger than gravitational ones. The capillary length is given by $l_{\rm c} = \sqrt{\gamma/(\rho g)} \simeq 1.5 \times 10^{-3}$ m. Therefore, in our system, the motion of the liquid inside the groove is driven by surface tension forces.

In Fig. 3 we plot a double logarithmic graph of the adimensional spread $(x - x_0)/l_{\rm c}$ over time t for different curvatures. The value x_0 is the initial spread adopted by the droplet inside the groove. One can notice that all long times dynamics are given by power laws as expected. But the slopes are different depending on the sign of the curvature. The spread of a droplet inside
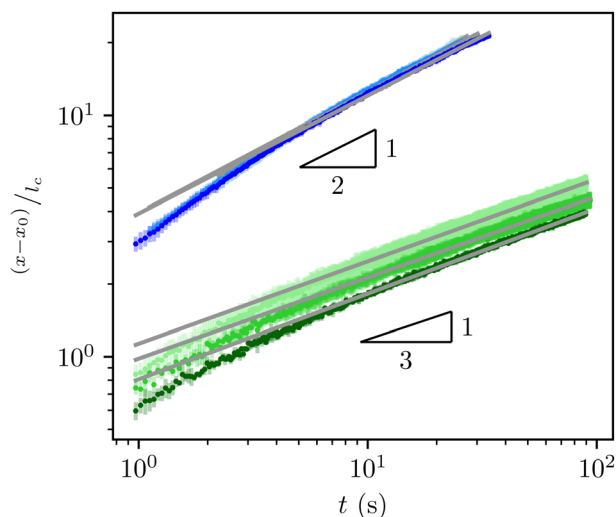
Fig. 3 Double logarithmic graph of the adimensional spread $(x - x_0)/l_c$ as function of time t. In blue, the groove is an epicycle. In green, the groove is a hypocycle. The darker the color is, the larger is the radius of the groove R (radius values are respectively 1.07 mm, 1.37 mm and 1.67 mm). The error bars coming from repeated experiments for each data set are in light color. One notices that the spread of a droplet inside an epicycle groove is independent of the radius R. However, for a hypocycle groove, the spread is faster for small radii. The grey lines are power law fits on experimental data, the fitting laws are described in Section 4.

Table 1 Table comparing studies about the scaling found for the spreading rate dynamics. Literature can be divided into two categories, studies with a reservoir that fills the structure (where the volume is not conserved) and studies with a droplet spreading on the structure (where the volume is constant). The exponent n is depending on the axial variation of the tube

Volume	Structure	Scaling
Not conserved	Cylindrical tube,[25,26,28] Porous substrate,[31–34] Rectangular groove,[29,30] Curved groove[30] Curved corners,[39,40]	$t^{1/2}$
	V-shaped groove,[41] Porous substrate[42]	$t^{1/3}$
	Diverging conical,[27] Converging conical[38]	t^n
Conserved	Rough substrate,[46,47] V-shaped groove,[48] Rectangular groove,[49] Micropillars substrate[33,51]	$t^{1/2}$
	Flat substrates,[43,44]	$t^{1/10}$
	Flat substrates,[45]	$t^{1/8}$
	Flat substrates[7]	$t^{1/7}$

an epicycle groove is going as time to the power one half. While inside a hypocycle groove, it spreads as time to the power one third. Then, we vary the radius R of the groove. We observe that the dynamic of a droplet inside an epicycle groove is independent of the radius as all curves collapse. However for a droplet inside a hypocycle groove, the spreading clearly depends on the radius of curvature. We observe that the spreading increases as the radius decreases. From those first observations, one can say that the spreading can be enhanced in a hypocycle groove with a small radius. Nevertheless, a droplet spreading inside an epicycle groove wins any droplet race, with spreading factors one order of magnitude larger than in the case of hypocycles.

4. Discussion

4.1 Previous studies

Many studies focus on capillary rises or droplet spreading along various surfaces.[7–10] All scaling obtained are summarized in Table 1. We divide the capillary driven motion into two categories, experiments with a reservoir where volume is not conserved *versus* experiments with a finite spreading volume.

In the first category, the liquid volume is not conserved due to the presence of a reservoir. When a cylindrical capillary tube touches the liquid reservoir, the liquid rises following a power law with an exponent 1/2. This relation is often referred as the Lucas–Washburn equation[25,26] or the Bell–Cameron–Lucas–Washburn (BCLW) equation, as Reyssat *et al.*[27] fairly pointed out that Bell and Cameron previously contributed to this topic.[28] This diffusive behavior was also found for invasion from a reservoir of rectangular[29] and curved grooves,[30] but also

for various pattern surfaces[31] or micropillars.[32–34] Subsequently, this diffusive behavior had been extended to dynamics of imbibing porous media going from textiles,[35] soils[36] to foams.[37] Other dynamics were also found. Reyssat[27] showed that depending on the axial variations in shape of divergent tubes, the exponent can be 1/4, 1/7 or even 1/10. Also, for different converging tubes, the exponent can be higher than 1/2.[38] When gravity affects the shape of the rising meniscus inside a corner, the power is 1/3 and is independent of the shape, whether it is curved corners[39,40] or V-shaped grooves.[41] For porous media, other textured surfaces showed a power of 1/3 as in the study of Obara *et al.*[42]

In the second category of situations, the spreading is limited by the droplet's volume conservation. On a smooth surface, if capillarity dominates the motion, the droplet spreads with a power law of time $t^{1/10}$, this scaling comes from Tanner's model.[43,44] Otherwise, when gravity overcomes capillarity, it spreads faster with a power 1/8.[45] When the dissipation at the contact line overcomes the bulk dissipation, the exponent is 1/7.[7] The roughness of the surface impacts the spreading, the power is within 0.25 and 0.5.[46,47] One can also add grooves on the surface, in such cases the droplet is confined inside the groove. For V-shaped grooves[48] and rectangular grooves[49] the power is 1/2. Also Warren calculated some powers depending on the geometry of the groove.[50] Droplets can also spread along a forest of micropillars,[33,51] in such cases the diffusion dynamics of Washburn is encountered.

From the Table 1, one can notice that a conserved volume can spread as fast as a filling with a reservoir if textures are added on the substrate. Grooves should be considered as a significant ingredient for droplet spreading. Therefore, it is not surprising to find such grooves in plants dealing with water scarcity, as shown in Fig. 1. One question remains, which

curvature sign is the best to spread a droplet inside a groove? From Section 3, we observe that the power is affected by the groove's curvature. To describe the dynamics, we proposed models for both cases. They are detailed below.

4.2 Hypocycle–concave

A droplet inside a hypocycle groove spreads along the direction given by the channel (see Fig. 2). This motion is led by surface tension acting along the contact line. The driving force can be expressed as

$$F_{\gamma,h} \sim \gamma x \theta_D{}^2 \tag{1}$$

where θ_D is the dynamical contact angle.[52] We can express this contact angle as $\theta_D \simeq z/R$, where z is the height of the droplet that decreases as the droplet spreads. In fact, as can be seen in Fig. 2(b), the front meniscus is curved. The characteristic length of this meniscus is assumed to be the radius of the groove R. Hence, the driving force is given by

$$F_{\gamma,h} \sim \gamma x \frac{z^2}{R^2} \tag{2}$$

Since the dissipation occurs in the bulk of the droplet, the dissipation force is then given by

$$F_{\eta,h} \sim \nu \rho x \dot{x} \tag{3}$$

where $\dot{x}$ is the spreading speed. By balancing both forces and looking the stationary equation, one can obtain the expression of the spreading speed, $\dot{x} \sim \frac{\gamma}{\nu \rho} \frac{z^2}{R^2}$. By assuming the volume of the droplet is $\Omega \sim xzR$. Therefore, the speed is expressed as $\dot{x} \sim \frac{\gamma}{\nu \rho} \frac{\Omega^2}{x^2 R^4}$. This leads to the following expression of the spread over time

$$x \sim \left(\frac{\gamma}{\nu \rho} \frac{\Omega^2}{R^4} t\right)^{1/3}. \tag{4}$$

This model is giving the scaling law to describe the spreading. It predicts a power law of time to the power one third as observed experimentally. In fact, this model is an adaptation of the Tanner's model that describes the spreading of a droplet on a smooth surface. Here, we have a 1D version of that model where the driving force as well as the volume of the droplet are rewritten to take into account the confinement of the droplet inside the 1D groove.

4.3 Epicycle–convex

A picture of a droplet spreading inside an epicycle groove is shown in Fig. 2(c). One can notice that the advancing contact line of the droplet is pinched at the cusp of the epicycle (Fig. 2(b)). There, the fastest spreading takes place, therefore this point dominates the dynamic. As the front meniscus is in contact with the cusp of the groove, the driving force is expressed as

$$F_{\gamma,e} \sim \gamma r_p \tag{5}$$

where r_p is the accuracy of the 3D printer. In fact, the advancing front is confined inside the bottom of the groove where the

characteristic length scale is fixed by the layer deposition accuracy of the 3D printer. In our system, we have $r_p \approx 30$ μm. The dissipation occurs in the bulk of the droplet. The dissipation force is thus given by

$$F_{\eta,e} \sim \nu \rho x \dot{x}. \tag{6}$$

The spread is obtained by balancing the forces. The expression of the spread x of the droplet over time is therefore given by

$$x \sim \left(\frac{\gamma}{\nu \rho} r_p t\right)^{1/2}. \tag{7}$$

This scaling model is based on the BCLW model. It corresponds to the case of a closed capillary tube with the size of the cusp r_p.

4.4 Analysis

In the previous sections we proposed two models for the spreading of a droplet inside each type of groove. We can fit the experimental data with the equations of each curvature (eqn (4) and (7)). The fitting law is a power law, $x = ct^p$ with two fitting parameters, being the coefficient c and the power p. In Fig. 3, the grey lines are the adjustment of the power law on the data. These fits capture the overall trend of the spreading process effectively. Please notice that the scaling law deviates from the experimental data during the initial seconds of the experiment. We attributed this deviation to a change in regime, the transition from the droplet filling the groove to a regime where the volume inside the groove is constant, as discussed in Section 2. The observed deviation is an indication of the time range during which the regime transition affects the dynamic. Our models describe the spreading behavior for a constant volume, which is applicable to later time periods.

In Fig. 4, we plot a graph of the fitting parameter p, the power of the fitting power law, as function of the groove's radius R. For both the hypocycle and the epicycle groove, the parameter p is independent of the radius of the groove. We found a power one third for the hypocycle groove and a power one half for the epicycle. The models proposed in the previous subsections are in excellent agreement with the experimental data.

In Fig. 5, we plot a double logarithmic graph of the fitting parameter c as function of the groove's radius R for both curvatures. Firstly, for the hypocycle case, the coefficient c of the power law exhibits a decreasing trend with the radius R of the groove. This trend can itself be fitted,

$$c_h = a_h R^{-4/3} \tag{8}$$

with $a_h = 1.6$ mm$^{4/3}$ s$^{-1/3}$. The model proposed in Section 4.2 gives the eqn (4) where the spread is decreasing with the good dependency of the radius. We have

$$c_h = \frac{1}{l_c}\left(\frac{\gamma}{\nu \rho}\Omega^2\right)^{1/3} R^{-4/3}. \tag{9}$$

Then, the prefactor a_h provided by the model is $a_{h,model} = \frac{1}{l_c}\left(\frac{\gamma}{\nu \rho}\Omega^2\right)^{1/3} = 12$ mm$^{4/3}$ s$^{-1/3}$, it overestimates the experimental
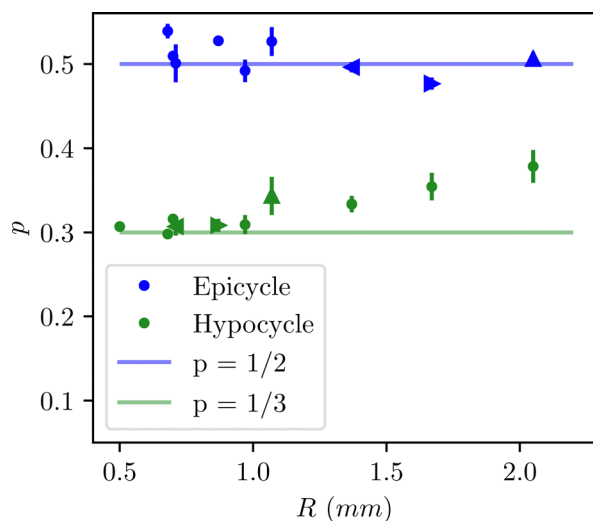
Fig. 4 The fitted exponent p as function of the radius R of the groove. For both curvatures, the exponent p is independent of the radius. It has two distinct values, one half for the epicycle and one third for the hypocycle. The triangular markers correspond to the same cross-section of the groove (left triangle $S = 0.8$ mm²; right triangle $S = 1.2$ mm²; up triangle $S = 1.8$ mm²).
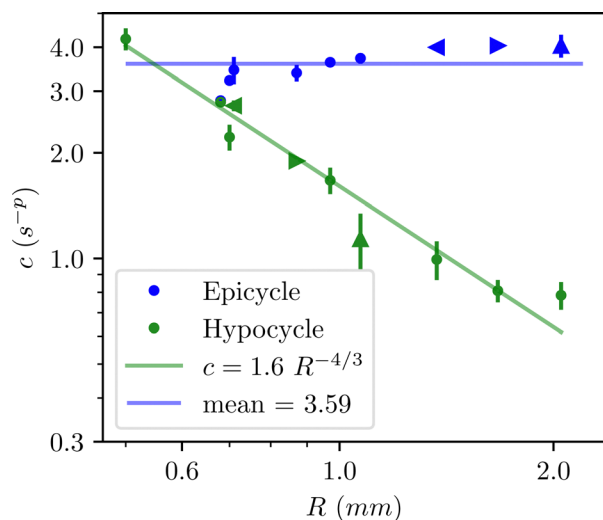
Fig. 5 Double logarithmic graph of the fitted prefactor c as function of the radius R of the groove. The error bars are smaller than the size of the symbols. For the epicycle, the parameter c is independent of the groove's radius. For the hypocycle, the parameter c follows a decreasing power law of the radius. The triangular markers correspond to the same cross-section of the groove (left triangle $S = 0.8$ mm²; right triangle $S = 1.2$ mm²; up triangle $S = 1.8$ mm²).

value as no geometrical factors were taken into account in our model. Nevertheless, the model gives the good power as well as the right dependency for R.

Secondly, for the epicycle groove, the coefficient in front of the power law is independent of the radius of the groove. This can be understand as the droplet is pinched at the cusp of the groove where the characteristic length is governed by the

accuracy of the 3D printer. The model obtained in Section 4.3 gives the equation eqn (7) which recovers this independence of the groove's radius. We have

$$c_{\mathrm{e}} = \frac{1}{l_{\mathrm{c}}}\left(r_{\mathrm{p}}\frac{\gamma}{\nu\rho}\right)^{1/2}. \qquad (10)$$

The value of this coefficient is $c_{\mathrm{e}} = 1.7$ s$^{-1/2}$ which is the same order of magnitude as the mean value obtained in Fig. 5.

The influence of the cross section of the groove is depicted by the triangular markers in Fig. 4 and 5. One observes that these data can be analyzed by considering the radius of the groove.

The models explained in Sections 4.2 and 4.3 are in excellent agreement with the experimental data. In both cases, we use the expression of a bulk dissipation. The difference between both models appears in the expression of the driving force. This driving force takes into account the specific shape of the droplet adopted inside the groove. Different shapes lead to two distinct dynamics.

5. Application

To compare the spreading efficiency of both groove types, we have created the logo of our University with either epicycle grooves or hypocycle grooves. To compare both structures, we kept as a constant the cross section, $S = 0.8$ mm². Meaning the radius of the epicycle groove is larger than the hypocycle one. The experimental pictures are shown in Fig. 6. A droplet is dropped off at the same spot on both logos, the droplet is colored in black. After 170 s, the logo made with epicycle grooves is completely filled, and the logo is highlighted by
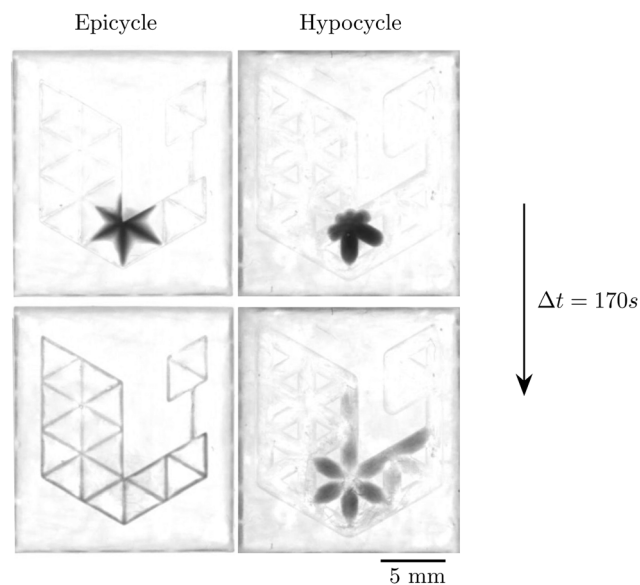
Fig. 6 The logo of the University of Liège is a triangular lattice. By using epicycle grooves (left) or hypocycle grooves (right), a droplet colored in black spreads inside the network. Both grooves have the same cross section, $S = 0.8$ mm² (epicycle's radius: $R = 1.37$ mm and hypocycle's radius: $R = 0.71$ mm). In the epicycle case, the logo is filled after 170 s. However, during this same lapse of time, the hypocycle logo is half filled.

the droplet. While, during this same lapse of time, the logo made with hypocycle grooves is more or less still half filled. This simple experiment proves that spreading can be enhanced using the right curvatures of the grooves. One could imagine microfluidics device based on this groove avoiding the use of pumps.

This research is in line with water collection problems. In fact, the findings of this study have potential applications in improving water collection in arid regions. Large meshes of cylindrical fibers show good efficiency in fog catching. The structure is made with either an intermingling of fibers[53,54] or with harps made of vertical fibers.[55,56] One could imagine to add curved grooves on the fibers in order to increase the drainage. In fact, the groove spreads the liquid and retains it as a film which should decrease the friction. Better than that, it has recently been showed that epicycloid structure of the fiber allows droplets to go down faster.[57] Moreover, the first step of any fog catcher is the initialization time, this is when the net is capturing liquid without draining it.[58] Simply by adding curved grooves on the fiber, this onset time should decrease.

6. Conclusion

A study of curved groove effect on the droplet spreading dynamics has been performed. A 3D printer is used to manufacture the grooves, it allows to choose easily the radius of curvature. A droplet spreading in a curved groove adopts a different shape depending on the sign of the curvature. Specifically, we observed that the advancing contact line is curved for the hypocycle groove (concave), while the front of the liquid is pinched inside the cusp of the groove for the epicycle (convex). This leads to different spreading dynamics. In both cases, the droplet spreads with a power law. For the hypocycle groove, the power is one third and the pre-factor decreases with the a power law of the groove's radius. For the epicycle groove, the power is one half, which is higher than the hypocycle case, and the pre-factor is independent of the groove's radius. We proposed two models inspired from Tanner's and BCLW's models that predict these powers and pre-factors. Notice that both powers encountered are greater than the one of a droplet spreading on a flat surface (power 1/10). Therefore, grooved structures favor any droplet spreading. Consequently it is not surprising to found such kind of structures on plants living in arid regions, as illustrated in Fig. 1.[11–13] Our study reveals that epicycle grooves are more efficient to spread droplets, with in the power law a higher exponent and a larger pre-factor. Epicycle grooves seems similar to the large bumps and small hollows observed on some natural fibers, see Fig. 1(a) and (c). Further biological research could verify this hypothesis. In conclusion, our study provides a comparison between two ways of spreading droplets and offers many new perspectives.

Author contributions

JVH has performed all experiments, data analysis and wrote the article. NV participated to data analysis and article writing.

Conflicts of interest

There are no conflicts to declare.

Acknowledgements

Notes and references

1 P. G. de Gennes, *Rev. Mod. Phys.*, 1995, **57**, 827–863.
2 A. Olanrewaju, M. Beaugrand, M. Yafia and D. Juncker, *Lab Chip*, 2018, **18**, 2323–2347.
3 T. Gilet, D. Terwagne and N. Vandewalle, *Appl. Phys. Lett.*, 2009, **95**, 014106.
4 M. M. Weislogel, *Adv. Space Res.*, 2003, **32**, 163–170.
5 D. Seo, J. Lee, C. Lee and Y. Nam, *Sci. Rep.*, 2016, **6**, 24276.
6 J. Ha and H.-Y. Kim, *Annu. Rev. Fluid Mech.*, 2020, **52**, 263–284.
7 J. D. Coninck, M. J. de Ruijter and M. Voué, *Curr. Opin. Colloid Interface Sci.*, 2001, **6**, 49–53.
8 G. Reiter, in *Spreading of Liquids on Substrates*, ed. L. F. M. da Silva, A. Öchsner and R. D. Adams, Springer International Publishing, Cham, 2017, pp. 1–13.
9 J. Cai, Y. Chen, Y. Liu, S. Li and C. Sun, *Adv. Colloid Interface Sci.*, 2022, **304**, 102654.
10 N. Kubochkin and T. Gambaryan-Roisman, *Curr. Opin. Colloid Interface Sci.*, 2022, **59**, 101575.
11 J. Ju, H. Bai, Y. Zheng, T. Zhao, R. Fang and L. Jiang, *Nat. Commun.*, 2012, **3**, 1247.
12 H. Chen, T. Ran, Y. Gan, J. Zhou, Y. Zhang, L. Zhang, D. Zhang and L. Jiang, *Nat. Mater.*, 2018, **17**, 935–942.
13 A. Roth-Nebelsick, M. Ebner, T. Miranda, V. Gottschalk, D. Voigt, S. Gorb, T. Stegmaier, J. Sarsour, M. Linke and W. Konrad, *J. R. Soc., Interface*, 2012, **9**, 1965–1974.
14 F. T. Malik, R. M. Clement, D. T. Gethin, W. Krawszik and A. R. Parker, *Bioinspir. Biomim.*, 2014, **9**, 031002.
15 D. Gurera and B. Bhushan, *Phil. Trans. R. Soc. A*, 2020, **378**, 20190444.
16 L. Zhang, G. Liu, H. Chen, X. Liu, T. Ran, Y. Zhang, Y. Gan and D. Zhang, *J. Bionic. Eng.*, 2021, **18**, 1–29.
17 E. Lorenceau and D. Quéré, *J. Fluid Mech.*, 2004, **510**, 29–45.
18 J. Van Hulle, F. Weyer, S. Dorbolo and N. Vandewalle, *Phys. Rev. Fluids*, 2021, **6**, 024501.
19 C. L. Lee, T. S. Chan, A. Carlson and K. Dalnoki-Veress, *Soft Matter*, 2022, **18**, 1364–1370.
20 M. Cao, J. Ju, K. Li, S. Dou, K. Liu and L. Jiang, *Adv. Funct. Mater.*, 2014, **24**, 3235–3240.
21 D. Gurera and B. Bhushan, *J. Colloid Interface Sci.*, 2019, **551**, 26–38.
22 H. Bai, T. Zhao, X. Wang, Y. Wu, K. Li, C. Yu, L. Jiang and M. Cao, *J. Mater. Chem. A*, 2020, **8**, 13452–13458.

23 B. Hu, Z. Duan, B. Xu, K. Zhang, Z. Tang, C. Lu, M. He, L. Jiang and H. Liu, *J. Am. Chem. Soc.*, 2020, **142**, 6111–6116.

24 Y. Li, Z. Cui, G. Li, H. Bai, R. Dai, Y. Zhou, Y. Jiao, Y. Song, Y. Yang, S. Liu and M. Cao, *Adv. Funct. Mater.*, 2022, **32**, 2201035.

25 V. R. Lucas, *Kolloid Zeistschrift*, 1918, **23**, 15–22.

26 E. W. Washburn, *Phys. Rev.*, 1921, **17**, 273–283.

27 M. Reyssat, L. Courbin, E. Reyssat and H. A. Stone, *J. Fluid Mech.*, 2008, **615**, 335–344.

28 J. M. Bell and F. K. Cameron, *J. Phys. Chem.*, 1906, **10**, 658–674.

29 P. Kolliopoulos, K. S. Jochem, D. Johnson, W. J. Suszynski, L. F. Francis and S. Kumar, *J. Fluid Mech.*, 2021, **911**, A32.

30 D. Yang, M. Krasowska, C. Priest, M. N. Popescu and J. Ralston, *J. Phys. Chem. C*, 2011, **115**, 18761–18769.

31 Y. Chen, L. S. Melvin, S. Rodriguez, D. Bell and M. M. Weislogel, *Microelectron. Eng.*, 2009, **86**, 1317–1320.

32 J. Bico, C. Tordeux and D. Quéré, *Europhys. Lett.*, 2001, **55**, 214–220.

33 C. Ishino, M. Reyssat, E. Reyssat, K. Okumura and D. Quéré, *EPL*, 2007, **79**, 56005.

34 B. Darbois Texier, P. Laurent, S. Stoukatch and S. Dorbolo, *Microfluid. Nanofluid.*, 2016, **20**, 53.

35 F. Ferrero, *Polym. Test.*, 2003, **22**, 571–578.

36 J. C. Ramírez-Flores, J. Bachmann and A. Marmur, *J. Hydrol.*, 2010, **382**, 10–19.

37 H. Caps, S. J. Cox, H. Decauwer, D. Weaire and N. Vandewalle, *Colloids Surf., A*, 2005, **261**, 131–134.

38 J.-B. Gorce, I. J. Hewitt and D. Vella, *Langmuir*, 2016, **32**, 1560–1567.

39 A. Ponomarenko, D. Quéré and C. Clanet, *J. Fluid Mech.*, 2011, **666**, 146–154.

40 J. Zhou and M. Doi, *J. Fluid Mech.*, 2020, **900**, A29.

41 D. Deng, Y. Tang, J. Zeng, S. Yang and H. Shao, *Int. J. Heat Mass Transf.*, 2014, **77**, 311–320.

42 N. Obara and K. Okumura, *Phys. Rev. E*, 2012, **86**, 020601.

43 L. H. Tanner, *J. Phys. D: Appl. Phys.*, 1979, **12**, 1473–1484.

44 A. E. Seaver and J. C. Berg, *J. Appl. Polym. Sci.*, 1994, **52**, 431–435.

45 J. Lopez, C. A. Miller and E. Ruckenstein, *J. Colloid Interface Sci.*, 1976, **56**, 460–468.

46 A. M. Cazabat and M. A. C. Stuart, *J. Phys. Chem.*, 1986, **90**, 5845–5849.

47 S. Dorbolo, *Pap. Phys.*, 2021, **13**, 130006.

48 R. R. Rye, J. A. Mann and F. G. Yost, *Langmuir*, 1996, **12**, 555–565.

49 T. Chen, *J. Termophys. Heat Transf.*, 2015, **29**, 594–601.

50 P. B. Warren, *Phys. Rev. E*, 2004, **69**, 041601.

51 L. Courbin, E. Denieul, E. Dressaire, M. Roper, A. Ajdari and H. A. Stone, *Nat. Mater.*, 2007, **6**, 661–664.

52 P. de Gennes, F. Brochard-Wyart and D. Quéré, *Gouttes, bulles, perles et ondes*, Belin, 2005.

53 J. de Dios Rivera, *Atmos. Res.*, 2011, **102**, 335–342.

54 K.-C. Park, S. S. Chhatre, S. Srinivasan, R. E. Cohen and G. H. McKinley, *Langmuir*, 2013, **29**, 13269–13277.

55 W. Shi, M. J. Anderson, J. B. Tulkoff, B. S. Kennedy and J. B. Boreyko, *ACS Appl. Mater. Interfaces*, 2018, **10**, 11979–11986.

56 N. G. Kowalski, W. Shi, B. S. Kennedy and J. B. Boreyko, *ACS Appl. Mater. Interfaces*, 2021, **13**, 38826–38834.

57 M. Leonard, J. Van Hulle, F. Weyer, D. Terwagne and N. Vandewalle, 2023, In preparation.

58 Y. Jiang, C. Machado, S. Savarirayan, N. A. Patankar and K.-C. Park, *Soft Matter*, 2019, **15**, 6779–6783.